Check for updates

Mechanism of synergistic removal of NO and SO$_2$ by sodium bicarbonate

Song Shu,[ab] Yiqi Huang,[c] Longhua Zou,[d] Xinyi Zhang[c] and Jianjun Li (ID) *[ab]

Sodium bicarbonate (NaHCO$_3$) is considered to be an effective alkaline adsorbent for SO$_2$ removal and surprisingly, the concentration of NO is significantly reduced along with the generation of NO$_2$ during its desulfurization. Unfortunately, the mechanism of NO interaction with NaHCO$_3$, SO$_2$ and O$_2$ is ambiguous. In this work, the effects of absorption gas and absorber composition on SO$_2$/NO absorption performance were explored, the absorption products were characterized using XPS and SEM, and the Gibbs free energy of the inferred reaction path was calculated based on density functional theory (DFT). The results showed that SO$_2$ and O$_2$ synergistically promoted the absorption and removal of NO by NaHCO$_3$, which could completely remove SO$_2$ and absorb 90% of NO at 160 °C. Sodium metabisulfite (Na$_2$S$_2$O$_5$) and sodium dithionate (Na$_2$S$_2$O$_6$) were identified as the active substances responsible for efficient NO absorption, and the oxidation of Na$_2$S$_2$O$_5$ to Na$_2$S$_2$O$_6$ is the controlling step of the NO removal reaction. Specifically, Na$_2$S$_2$O$_5$ is an intermediate produced by the reaction of NaHCO$_3$ with SO$_2$, and subsequently reacts with O$_2$ to produce Na$_2$S$_2$O$_6$, which releases reactive oxygen species to oxidize NO to NO$_2$. In addition, when the S/N ratio is greater than 1 and the O$_2$ content is greater than 5%, both SO$_2$ and NO can maintain removal efficiency higher than 90%, indicating that the absorption reaction of SO$_2$ and NO by NaHCO$_3$ is highly adaptable to the flue gas composition.

1. Introduction

As the world's population and energy demand increase, continued industrialization will undoubtedly raise the levels of atmospheric pollutants, such as SO$_2$ and NO, which are harmful to the environment and human health. Flue gas desulfurization (FGD) and ammonia-based selective catalytic reduction (NH$_3$-SCR) denitrification are simultaneously applied for controlling pollutant emissions in power plants.[1–3] However, desulfurization performed using wet sorbents requires large installation space, large amounts of water and high capital as well as operating costs,[4–6] and research has shifted toward dry methods of SO$_2$ removal. Various types of solid sorbents/catalysts are being used for dry FGD, like calcium based,[2] sodium based,[7,8] activated carbon,[9,10] and metal oxide.[11] Among the dry sorption, sodium bicarbonate (NaHCO$_3$) has attracted particular interest because of its ability to produce valuable solid compounds with SO$_2$, such as sodium sulfite and sulfate, which can be used as alkali agent, anti-caking agent and neutralizer. In addition, NaHCO$_3$ as a SO$_2$ dry-sorbent can couple cost-effectiveness and

environmental compatibility in practical engineering applications, and it has been implemented in a great number of plants in Europe.[12–15]

Surprisingly, the concentration of NO$_x$ was simultaneously reduced during the desulfurization with NaHCO$_3$,[16] providing the possibility to realize integrated removal of multiple pollutants in a single system. Barbara Walawska *et al.* stated that the efficiency of NaHCO$_3$ for NO$_x$ removal was about 21% at 300 °C,[17] but failed in the absence of SO$_2$. It was presumed that the intermediate of Na/SO$_x$ generated by the desulfurization reaction plays a key role in NO removal, especially sodium metabisulfite (Na$_2$S$_2$O$_5$). Unfortunately, the efficient Na/SO$_x$ intermediates are still ambiguous and the synergistic removal mechanisms of SO$_2$ and NO$_x$ are currently lacking in research.

In this work, the effect of gas composition on the absorption of SO$_2$ and NO by NaHCO$_3$ was investigated using a fixed-bed reactor. The Na/SO$_x$ intermediates generated by the FGD process were characterized by scanning electron microscopy (SEM) and X-ray photoelectron spectroscopy (XPS), and then the adsorption properties of a series of possible Na/SO$_x$ on SO$_2$ and NO were examined. Furthermore, the effects of O$_2$ in NO oxidation and Na/SO$_x$ formation was evaluated. Most interestingly, the reaction paths were inferred from density functional theory (DFT) calculations of Gibbs freedom to elucidate the mechanism of NO and SO$_2$ removal by Na/SO$_x$. Overall, we pave the way for the development of NaHCO$_3$ for simultaneous desulfurization and denitrification.

[a] College of Carbon Neutrality Future Technology, Sichuan University, Chengdu 610065, China. E-mail: jjli@scu.edu.cn

[b] National Engineering Research Center for Flue Gas Desulfurization, Chengdu 610065, China

[c] College of Architecture and Environment, Sichuan University, Chengdu 610065, China

[d] College of Food and Biological Engineering, Chengdu University, Chengdu 610106, China

2. Materials and methods

2.1 Materials

The analytical grade of $NaHCO_3$ with mean diameter of 50–100 μm, sodium carbonate (Na_2CO_3), sodium bisulfite ($NaHSO_3$), sodium sulfite (Na_2SO_3) and $Na_2S_2O_5$ were all purchased by Kelong Company. $Na_2S_2O_6$, which is in science labs, was synthesized by the following chemical method:

$$MnO_2 + 2SO_2 = MnS_2O_6 \qquad (1)$$

$$MnS_2O_6 + Na_2CO_3 = Na_2S_2O_6 + MnCO_3 \qquad (2)$$
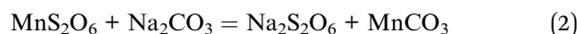
2.2 Experimental sections

The experiments were carried out in the fixed-bed reactor with a diameter of 2 cm and a height of 1.6 cm at ambient, depicted schematically in Fig. 1. The simulated flue gas consisted of SO_2, NO, O_2 and N_2, supplied by a compressed cylinder and metered by a mass flow controller. The concentration of the gas compositions in the inlet and outlet flows was monitored by a flue gas analyzer (Testo 350, Germany). The temperature inside the bed was controlled by thermocouples.

To investigate the synergy effects on the adsorption of SO_2 and NO by $NaHCO_3$, individual and simultaneous sorption process were designed. The uniform reaction conditions set for SO_2 and NO adsorption by $NaHCO_3$ included $T = 160$ °C, GHSV $= 10\ 000\ h^{-1}$, flow rate $= 1$ L min^{-1}, 5 vol% O_2 and adsorption residence time of 60 min. The composition of the adsorption gas was adjusted as a variable and its specific names are listed in Table 1.
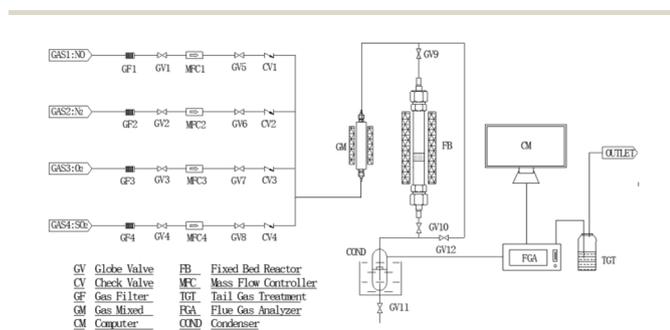

Fig. 1 Schematic diagram of the fixed-bed laboratory apparatus.

Table 1 The named samples corresponding to the specific gas compositions

	Gas compositions	
Sample	0–30 min	31–60 min
S550N0	550 ppm SO_2	
N500S0	500 ppm NO	
S550/N500	550 ppm SO_2	500 ppm NO
S550-N500	550 ppm SO_2	550 ppm SO_2 + 500 ppm NO
N500-S550	500 ppm NO	500 ppm NO + 550 ppm SO_2
S550N500	550 ppm SO_2 + 500 ppm NO	

The desulfurization and denitration properties of the possibility Na/SO_x included Na_2CO_3, $NaHSO_3$, Na_2SO_3, $Na_2S_2O_5$, and $Na_2S_2O_6$ were than examined, respectively. Since $NaHSO_3$ and $Na_2S_2O_5$ would release SO_2 at 160 °C according to the results of pre-experiments, $NaHSO_3$ and $Na_2S_2O_5$ as additives were set in the ratios of 1 : 4 with $NaHCO_3$ to measure their effects on NO removal. In addition, the role of O_2 in the oxidation of NO was investigated by coexisting/not coexisting O_2 in the sorption gas.

2.3 Characterization methods

The thermal decomposition properties were characterized using an SDTQ600 instrument (TA Instruments, USA) at a heating rate of 5 °C min^{-1} to 200 °C and a N_2 flow rate of 100 mL min^{-1}. The specific surface areas were calculated by the Brunauer–Emmett–Teller (BET) method, and the pore sizes and pore capacities were calculated by the Barrett–Joyner–Halenda (BJH) method. SEM images of sorbent particle were performed using a JSM-7500F scanning electron microscope (JEOL Japan) at an acceleration voltage of 5 kV. X-ray photoelectron spectra (XPS) with Al Kα source carried out on a Thermo ESCALAB250Xi instrument was used to characterize and semi-quantify the chemical compositions of reacted Na/SO_x.

2.4 Computational section

To identify the differences in Gibbs free energy (ΔG) of the reactions involved, Density Functional Theory (DFT) calculations were performed with VASP 5.3.5 code.[18,19] Generalized gradient approximation with Perdew–Burke–Ernzerhof exchange and correlation functional were used.[20] A plane-wave basis set of 400 eV cut off energy was employed in the framework of projector-augmented wave method.[21] The Gaussian smearing with a width of 0.2 eV was used. The convergence criteria for the energy and force were set to 10^{-5} eV and 0.01 eV Å^{-1}. ΔG is calculated as the following:

$$\Delta G = G_{product} - G_{reactant} \qquad (3)$$

where the $G_{product}$ and $G_{reactant}$ represent Gibbs free energies of products and reactants, respectively. The Gibbs free energies of gas phase can be calculated as the eqn (5):[22]

$$G_g(T,P) = E_{DFT}(K^0, P^0) + \Delta H_g(K^0 \rightarrow T, P^0) - TS_g(T, P^0) \qquad (4)$$

where the first term is the energy calculated by DFT, and the second and the third terms are the contribution of gas enthalpy and entropy under standard state pressure ($P^0 = 0.1$ MPa), respectively.

3. Results and discussion

3.1 Thermal decomposition properties of $NaHCO_3$

The Fig. 2A shows that $NaHCO_3$ decomposes at 80–160 °C, with the fastest rate of decomposition at 145 °C, while the weight loss at 80 °C corresponds to the separation of bound water.[23] The thermal decomposition process of $NaHCO_3$ is an active development, which is shown in the SEM images (Fig. 2B). As seen in
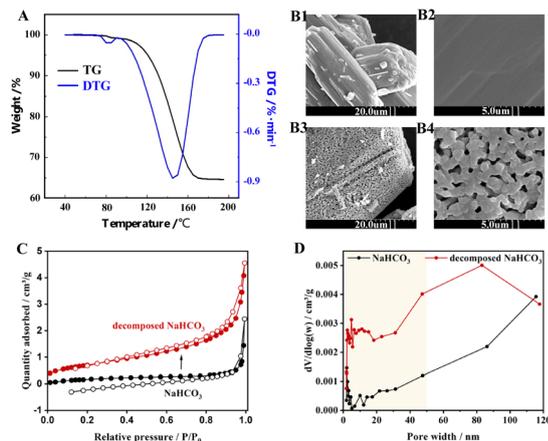
Fig. 2 (A) TG/DTG curves of $NaHCO_3$ at a heating rate of 5 °C min^{-1}. SEM images of (B1 and B2) $NaHCO_3$, and (B3 and B4) $NaHCO_3$ thermally decomposed at 160 °C. (C) Nitrogen adsorption–desorption isotherm and (D) pore size distribution of pristine and 160 °C decomposed $NaHCO_3$.

Fig. 3 SO_2/NO adsorption properties. $T = 160$ °C, GHSV = 10 000 h^{-1}, flow rate = 1 L min^{-1} and the total sorption time is 60 min. Single-component absorption experiments: (A1) S550N0, (B1) S0N500 and (C1) S550/N500. Simultaneous adsorption of SO_2 and NO: (A) S550-N500, (B2) N500-S550 and (C2) S550N500.

Fig. 2B1 and B2, the physical structure of the initial $NaHCO_3$ particles is nonporous, while the decomposed $NaHCO_3$ in Fig. 2B3 and B4 produces some visible micro-grade pores of about 1 μm. BET measurements were further carried out to characterize the pore structure of $NaHCO_3$. The N_2 adsorption–desorption isotherm results of are shown in Fig. 2C, where the specific surface area of $NaHCO_3$ increases from 0.7 to 2.4 m^2 g^{-1} after thermal decomposition at 160 °C, which is consistent with the shrinkage nucleation model.[24] The results of the pore size distribution in Fig. 2D indicate that the thermal decomposition of $NaHCO_3$ favours the formation of multistage pores, and these well-developed pore structures are expected to provide channels and sites for the physical and chemisorption of SO_2/NO.

3.2 Performance of $NaHCO_3$ in absorbing SO_2/NO

To investigate the effect of SO_2 on the absorption of NO by $NaHCO_3$, a series of single-component absorption experiments were first carried out and the results correspond to Fig. 3. In Fig. 3A1, the concentration of SO_2 drops sharply to 0 at the beginning of the reaction for 10 min, and remains complete absorption until the end of the reaction, indicating the dominance of $NaHCO_3$ in desulfurization. However, the concentration of NO in Fig. 3B1 decreases from 500 to 400 ppm at most and then rises to 500 ppm, implying that the individual uptake of NO by $NaHCO_3$ is weak and occurs mainly through physical adsorption and the spontaneous reaction of NO oxidation to NO_2. On this basis, a performance test (Fig. 3C1) was conducted with pre-sorption of SO_2 followed by NO adsorption, resulting in no decrease in NO concentration after stopping SO_2 injection. The above results show that $NaHCO_3$ has good SO_2 absorption performance, but it is ineffective for single NO absorption, and pre-absorption of SO_2 has no effect on NO absorption by $NaHCO_3$.

The sorption performance of the S550-N500, N500-S550 and S550N500 samples with SO_2 and NO coexisting was shown in

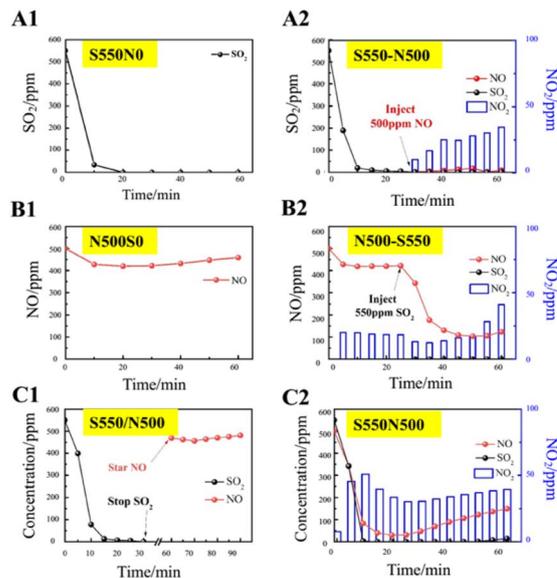Fig. 3A2, B2 and C2. It is easily found that the coexistence of SO_2 significantly promotes the absorption and conversion of NO and increase the production of NO_2, inferring that the Na/SO_x intermediates produced by the reaction of SO_2 with $NaHCO_3$ as active substances stimulate the absorption of NO. When NO is exposed to 550 ppm of SO_2 (Fig. 3A2), the NO concentrations immediately decrease to 0 ppm, while a maximum of about 35 ppm of NO_2 is detected in 30 min. The date in Fig. 3B2 show that when SO_2 is introduced into the NO being absorbed, the concentration of SO_2 rapidly drops to 0 ppm and the concentration of NO followed down to a minimum of 100 ppm accompanied by an increase in the concentration of NO_2 from 20 to 40 ppm. Similarly, as shown in Fig. 3C2, the concentration of SO_2 decreases faster than that of NO when SO_2 and NO are in contact with $NaHCO_3$ at the same time, and the absorption of SO_2 is significantly higher than that of NO, which indicates that $NaHCO_3$ preferentially absorbs SO_2 relative to NO.

Another finding is that the amount of NO_2 present is much smaller than the amount of NO absorbed, implying that a large number of nitrogenous species are stored in the absorber. The distribution of nitrogen species given in Fig. 4A for other nitrogenous species exceeds 60% of the NO feeding, indicating that the S550N500 absorber removes NO mainly through the formation of other nitrogenous species. However, it is uncertain whether NO_2 is an active intermediate species for NO removal, so experiments of mixed NO_2 and SO_2 removal were conducted. The results in Fig. 4b show that the NO_2 concentration is reduced from 360 to 140 ppm with 60% removal when SO_2 is coexisted and this implies that $NaHCO_3$ has good absorption properties for NO_2. Therefore, NO_2 is an important intermediate for NO removal, and it is the unabsorbed NO_2 that is detected in the gas.
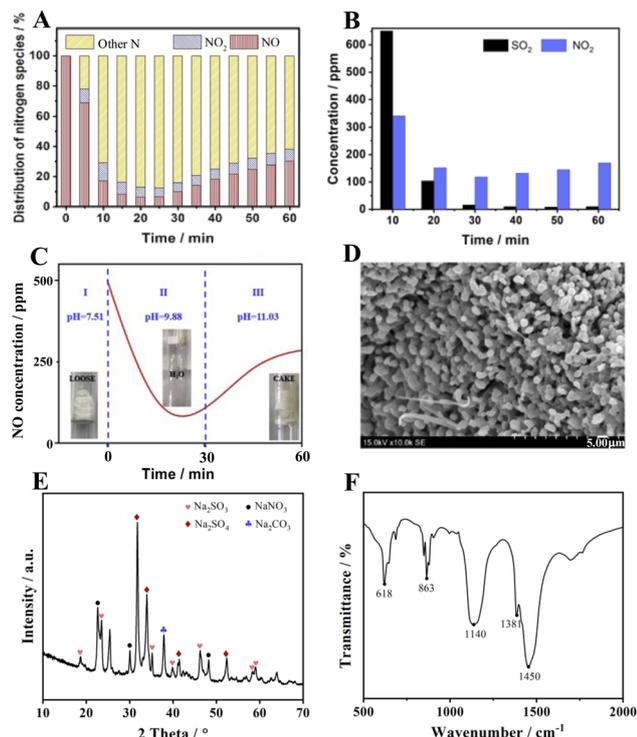
Fig. 4 (A) Nitrogen species distribution of NO absorbed by S550N500, (B) absorption properties of NO_2 in the coexistence of SO_2, (C) pH evolution of the absorption process of S550N500, (D) SEM image, (E) XRD spectra and (F) FTIR spectra of the absorber S550N500 after reaction with SO_2 and NO.

In addition, the changes in absorber morphology and pH were also recorded, and the results are shown in Fig. 4C. The unreacted $NaHCO_3$ is a loose, weakly basic salt with a pH of 7.51. When the reaction proceeds for 30 min, a large amount of water mist appears in the tube due to the release of water molecules from the thermal decomposition of $NaHCO_3$, at which time the pH is 9.88. It is noteworthy that the best NO removal efficiency is achieved at this time. As the reaction is prolonged, the absorber gradually condenses into lumps as the pH increases to 11.0, leading to a decrease in NO absorption performance. The SEM image of S550N500 after reaction with SO_2 and NO is shown in Fig. 4D. Unlike the morphology of $NaHCO_3$ after thermal decomposition, crystalline products cover the surface of S550N500, confirming the occurrence of the chemisorption reaction.

The XRD data of the absorption products are shown in Fig. 4E, and not surprisingly, Na_2CO_3, the thermal decomposition product of $NaHCO_3$, is detected at 37.8°. The characteristic peaks of Na_2SO_3 (JCPD 37-1488) appear at 18.7°, 23.5°, 35.2°, 40.0°, 46.4°, 58.3° and 59.1°, which are easily oxidized to Na_2SO_4 with $2\theta = 31.8°$, 33.9°, 41.4°, and 52.3° (JCPD 37-1475). In addition, diffraction peaks located at 22.6°, 30.1° and 48.2° are attributed to $NaNO_3$ according to JCPD 36-1474, confirming the chemical reaction between NO and the absorbent.

Fig. 4F shows the FTIR spectra of the samples after the absorption reaction. In addition to the peaks of Na_2CO_3 at 863

and 1450 cm^{-1}, the characteristic peaks corresponding to Na_2SO_4 appear at 618 and 1140 cm^{-1}, while that of $NaNO_3$ is at 1381 cm^{-1}, implying that the reaction products of $NaHCO_3$ with SO_2 and NO mainly include Na_2CO_3, Na_2SO_4 and $NaNO_3$.[25–27]

The reaction products were then characterized by XPS, and the high-resolution spectra of S 2p and N 1s were illustrated in Fig. 5. For S 2p, the peaks with binding energy located at 166.7 ± 0.2 eV can be attributed to Na_2SO_3 and $NaHSO_3$, while the peaks at 168.8 eV correspond to the mixed $Na_2S_2O_5$ and $Na_2S_2O_6$,[28–30] which are generated by the following eqn (6)–(13).[31] In addition, two characteristic peaks corresponding to the product Na_2SO_4 (Na_2SO_4 (1) and Na_2SO_4 (2)) are found at 168.4 eV and 169.6 eV, respectively.[32] This is consistent with Tim C. Keener that $NaHCO_3$ can react directly with SO_2 or with SO_2 after thermal decomposition, which gives rise to a multi-path reaction scheme between $NaHCO_3$ and SO_2 with temperature-sensitive properties.[24,33] When the reaction temperature reaches 413 K, the formation of Na_2SO_4 (1) by SO_2 uptake occurs mainly in the Na_2CO_3 micropores produced by the thermal decomposition of $NaHCO_3$,[8] and the amount of this Na_2SO_4 production is huge, accounting for 61% of the total S of S550N0. Moreover, Na_2SO_4 (2) located at 169.6 eV can be reasonably attributed to the direct reaction generation at the S550N0 surface with a percentage of about 4.4%.

For S550-N500, N500-S550 and S550N500, four forms of sulfur species existed after simultaneously absorption of SO_2 and NO, including two types of Na_2SO_4, $Na_2S_2O_5$ and $Na_2S_2O_6$, with $Na_2S_2O_6$ and Na_2SO_4 (2) predominating. However, the introduction of NO affects the distribution of sulfur species. Notably, when NO is present in the absorbed gas, Na_2SO_3/ $NaHSO_3$ disappears while Na_2SO_4 (2) is enriched, indicating that the conversion of SO_3^{2-} to SO_4^{2-} is promoted.

The N 1s XPS spectra given in Fig. 5B can distinguish two typical components with peaks located at 407.3 eV and 403.9 eV, which belong to sodium nitrate ($NaNO_3$) and sodium nitrite ($NaNO_2$), respectively.[34,35] Combined with the absorption performance of NO in the coexistence of SO_2 in Fig. 3, it is confirmed that the main products of NO conversion are nitrate nitrogen (NO_2^- and NO_3^-).
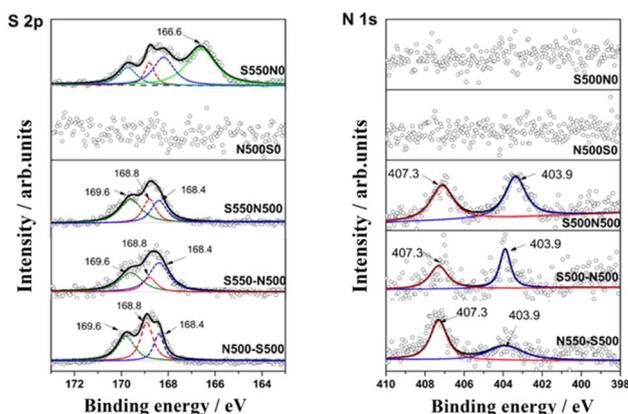

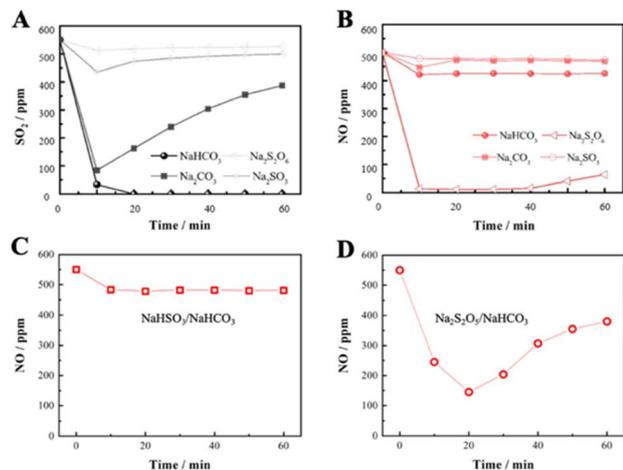**Fig. 5** Fitted S 2p and N 1s spectra of S550N0, N500S0, S550-N500, N500-S550 and S550N500.

Fig. 6 (A) Desulfurization performance of $NaHCO_3$, Na_2CO_3, Na_2SO_3, and $Na_2S_2O_6$. (B) Denitrification performance $NaHCO_3$, Na_2CO_3, Na_2SO_3 and $Na_2S_2O_6$. (C) Denitrification performance $NaHSO_3$/$NaHCO_3$. (D) Denitrification performance $Na_2S_2O_5$/$NaHCO_3$.

3.3 Performance of Na/SO_x in absorbing NO

Based on the above, the desulfurization/denitrification performance of specific intermediates was further investigated, including Na_2CO_3, Na_2SO_3 and $Na_2S_2O_6$. From Fig. 6A, $NaHCO_3$ is the best absorbent for desulfurization, and Na_2CO_3 is easily saturated by SO_2 adsorption, while the desulfurization efficiency of Na_2SO_3 and $Na_2S_2O_6$ is poor. During denitrification, as shown in Fig. 6B, $Na_2S_2O_6$ is the only effective absorber that can immediately react with NO and maintain prolonged uptake of NO. This indicates that $Na_2S_2O_6$ generated by the desulfurization is mainly responsible for the absorption reaction of NO. Further, an absorber with a 1 : 4 ratio of $NaHSO_3$ or $Na_2S_2O_5$ to $NaHCO_3$ was configured for probing its absorption activity of NO. As shown in Fig. 6C and D, $NaHSO_3$ has almost no denitrification activity, while $Na_2S_2O_5$ performs well in absorbing NO, reducing the concentration from 550 to 150 ppm. According to eqn (7)–(12), $Na_2S_2O_5$ as a reactant can produce $Na_2S_2O_6$, which promotes the absorption and conversion of NO.

3.4 Effect of O_2 on the absorption of SO_2 and NO

The role of O_2 in NO and SO_2 adsorption and removal was further investigated. The results in Fig. 7A show that without O_2,
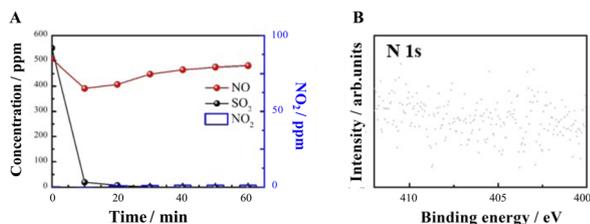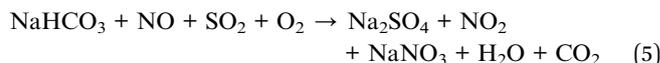

Fig. 7 SO_2 and NO uptake on $NaHCO_3$ in the absence of O_2. (A) $T = 160$ °C, GHSV $= 10\,000$ h^{-1}, flow rate $= 1$ L min^{-1}, $SO_2 = 550$ ppm, NO $= 500$ ppm, $O_2 = 0$ vol% and the total sorption time is 60 min. (B) Fitted N 1s spectra.

SO_2 sorption is not affected, but NO removal and NO_2 generation are significantly inhibited. XPS results (Fig. 7B) show that both NO_2^- and NO_3^- are not generated in the absence of O_2, speculating O_2 is necessary for the synergistic removal of NO by SO_2 and $NaHCO_3$.
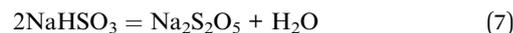
3.5 Gibbs free energy of reactions

For the possible intermediate species and reaction pathways involved in the process of SO_2 and NO uptake by $NaHCO_3$, the following schematic diagram 8 and eqn (5)–(14) are described, and the relevant Gibbs free energy (ΔG) is calculated.
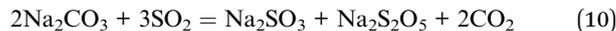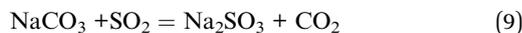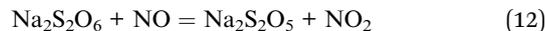
Overall reaction:

$$NaHCO_3 + NO + SO_2 + O_2 \rightarrow Na_2SO_4 + NO_2 + NaNO_3 + H_2O + CO_2 \quad (5)$$

Step A:

$$NaHCO_3 + SO_2 = NaHSO_3 + CO_2 \quad (6)$$

$$2NaHSO_3 = Na_2S_2O_5 + H_2O \quad (7)$$

Step B:

$$2NaHCO_3 \triangleq Na_2CO_3 + H_2O + CO_2 \quad (8)$$

$$NaCO_3 + SO_2 = Na_2SO_3 + CO_2 \quad (9)$$

$$2Na_2CO_3 + 3SO_2 = Na_2SO_3 + Na_2S_2O_5 + 2CO_2 \quad (10)$$

Step C:

$$2Na_2S_2O_5 + O_2 \leftrightarrows 2Na_2S_2O_6 \quad (11)$$

$$Na_2S_2O_6 + NO = Na_2S_2O_5 + NO_2 \quad (12)$$

$$Na_2S_2O_5 = Na_2SO_3 + SO_2 \quad (13)$$

Step D:

$$2NaHCO_3 + 2NO_2 = NaNO_2 + NaNO_3 + 2CO_2 + H_2O \quad (14)$$
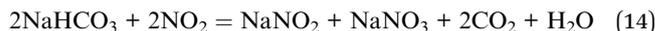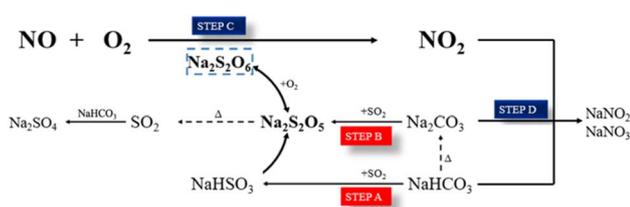
The generation of $Na_2S_2O_5$ from $NaHCO_3$ during desulfurization is thermodynamically favorable, and steps A and B are considered as two possible reactions with ΔG of -3276 and -5105 kJ mol^{-1}, respectively. Step B shows that the generation of $Na_2S_2O_5$ from Na_2CO_3 is also thermodynamically feasible, which ΔG is about -1281 kJ mol^{-1}. This indicates that $NaHCO_3$ can be directly or thermally decomposed into Na_2CO_3 to react with SO_2 to form $Na_2S_2O_5$. Steps C and D, as key steps in NO removal, describe the oxidation of NO to NO_2 by O_2 and $Na_2S_2O_5$ and further conversion of NO_2 to NO_X^- with ΔG of 675 kJ mol^{-1} (11), -158 kJ mol^{-1} (12), -858 kJ mol^{-1} (13) and -1721 kJ mol^{-1} (14), respectively. This means that the oxidation of $Na_2S_2O_5$ to $Na_2S_2O_6$ is the controlling step of the whole reaction (Table 2).

In summary, pathways A and B describe the chemical interaction between $NaHCO_3$ and SO_2 to produce the intermediate $Na_2S_2O_5$. According to path C, the reaction properties of

Table 2 The standard molar Gibbs energy ($\Delta_f G°$) of solid phase species,[36] and the standard entropy and enthalpy data are referred to thermochemical tables at $p^0 = 0.1$ Mpa, $T = 500$ K in website http://kinetics.nist.gov/janaf/. The energetics and Gibbs free energy of gas phase specie (E_{DFT}) are obtained by DFT calculations

Structure	$\Delta_f G°$ kJ mol^{-1}	Structure	E_{DFT} eV	ΔH_g(0 K → 500 K,P^0) kJ mol^{-1}	$S_g(T,P^0)$ J mol^{-1} K^{-1}	G_g(500 K,P^0) kJ mol^{-1}
NaHCO$_3$	−852	O$_2$	−9.8	4.34	172.20	−1031.2
Na$_2$CO$_3$	−1048	SO$_2$	−11.0	8.76	270.49	−1200
Na$_2$SO$_3$	−1012	NO	−12.2	6.06	226.26	−1290.4
Na$_2$SO$_4$	−1270	NO$_2$	−15.5	8.1	260.64	−1626.4
NaNO$_2$	−285	H$_2$O	−13.6	6.92	206.53	−1415.8
NaNO$_3$	−367	CO$_2$	−22.7	8.30	234.90	−2304.9
Na$_2$S$_2$O$_5$	−1354	N$_2$	−16.4	5.91	206.74	−1683.7
Na$_2$S$_2$O$_6$	−1532					

Fig. 8 A proposed reaction mechanism.

NaHCO$_3$ with NO depend on the formation of Na$_2$S$_2$O$_6$ from Na$_2$S$_2$O$_5$. The NO molecule acts as a Lewis acid and reacts on the surface of Na$_2$S$_2$O$_6$ to form NO$_2$.[37] Gradually, the generated NO$_2$ achieves a dynamic equilibrium of adsorption–desorption, and then reacts with NaHCO$_3$ to form NO$_x^-$. The removal mechanism and reaction pathway are shown in Fig. 8.

Considering that SO$_2$ and O$_2$ are the key factors that synergistically promote NO absorption, it is necessary to optimize the content of coexisting SO$_2$ and O$_2$ for improving the NO absorption performance. The ration of SO$_2$ and NO (S/N) of the absorbed gases are set to 0.5, 1, 2, 3, and 4, respectively, where the NO concentration is fixed at 500 ppm and the SO$_2$ concentration corresponds to 250, 500, 1000, 1500, and 2000 ppm. The results in Fig. 9A show that S/N has a small effect on the SO$_2$ removal, which is maintained above 95%. However, the efficiency of NO removal is only 34% when S/N is 0.5, which is considered that the oxidative absorption of NO is limited by the small number of reactive intermediates generated on the absorber surface. With S/N higher than 1, the absorption efficiency of NO is stabilized at about 90%. As the S/N increases to

1, the NO removal stabilizes to about 90%, emphasizing the necessity of SO$_2$ for NO absorption. As shown in Fig. 9B, the O$_2$ concentration does not affect the SO$_2$ absorption efficiency, which is always maintained at about 100%. However, when the O$_2$ content is increased from 0 to 5%, the NO removal efficiency dramatically increases from 11% to about 91%, and increasing the content of O$_2$ to 20% has no significant effect on the NO removal. Therefore, the NO removal by NaHCO$_3$ has the advantage of being highly adaptable to SO$_2$ and O$_2$ content of flue gas.

4. Conclusions

The NaHCO$_3$ simultaneous removal of SO$_2$ and NO perform a good activity. NaHCO$_3$ can completely adsorb SO$_2$ and absorb 90% of NO at 160 °C. The NO oxidation observed after the reaction with SO$_2$ and NaHCO$_3$ is due to the formation of Na/SO$_x$ species. The most likely reactive Na/SO$_x$ demonstrated theoretically and experimentally include Na$_2$S$_2$O$_6$ and Na$_2$S$_2$O$_5$. In addition, coexisting SO$_2$ and O$_2$ are the main factors for forming Na/SO$_x$. The Na$_2$S$_2$O$_5$ formed by the reaction of SO$_2$ with NaHCO$_3$ further reacts with O$_2$ to form Na$_2$S$_2$O$_6$, which could significantly alter the overall rate of the NO oxidation. Mechanistic studies have shown that the oxidation of NO to NO$_2$ is the key step for its efficient uptake and requires additional energy. This study clearly demonstrates the removal of NO by NaHCO$_3$ in the presence of SO$_2$ and O$_2$, which will be instructive for the synergistic removal of SO$_2$ and NO.

Conflicts of interest

There are no conflicts to declare.

Acknowledgements

Notes and references

1 Y. Zhao, T. Guo, Z. Chen and Y. Du, *Chem. Eng. J.*, 2010, **160**, 42–47.

Fig. 9 Effect of (A) the ration of SO$_2$ and NO and (B) the content of O$_2$ on the adsorption of SO$_2$ and NO.

© 2023 The Author(s). Published by the Royal Society of Chemistry

2 C.-F. Liu and S.-M. Shih, *Ind. Eng. Chem. Res.*, 2006, **45**, 8765–8769.

3 Y. Liu, W. Xu, L. Zhao, Y. Wang and J. Zhang, *Energy Fuels*, 2017, **31**, 12364–12375.

4 A. G. Chmielewski, E. Zwolińska, J. Licki, Y. Sun, Z. Zimek and S. Bułka, *Radiat. Phys. Chem.*, 2018, **144**, 1–7.

5 R.-B. Lin, S.-M. Shih and C.-F. Liu, *Chem. Eng. Sci.*, 2003, **58**, 3659–3668.

6 J.-H. Park, J.-W. Ahn, K.-H. Kim and Y.-S. Son, *Chem. Eng. J.*, 2019, **355**, 351–366.

7 I. Bahrabadi-Jovein, S. Seddighi and J. Bashtani, *Energy Fuels*, 2017, **31**, 14007–14017.

8 C. Wu, S.-J. Khang, T. C. Keener and S.-K. Lee, *Adv. Environ. Res.*, 2004, **8**, 655–666.

9 S. Wang, S. Xu, S. Gao, P. Xiao, M. Jiang, H. Zhao, B. Huang, L. Liu, H. Niu, J. Wang and D. Guo, *Sci. Rep.*, 2021, **11**, 11003.

10 L. Xu, J. Guo, F. Jin and H. Zeng, *Chemosphere*, 2006, **62**, 823–826.

11 R. Sundararaman and C. Song, *Energy Fuels*, 2013, **27**, 6372–6376.

12 A. Dal Pozzo, D. Guglielmi, G. Antonioni and A. Tugnoli, *J. Cleaner Prod.*, 2017, **162**, 1061–1074.

13 J. Vehlow, *Waste Manage.*, 2015, **37**, 58–74.

14 M. A. Paisley and M. Millspaugh, in *19th Annual North American Waste-to-Energy Conference*, ASMEDC, Lancaster, Pennsylvania, USA, 2011, pp. 1–8.

15 S. Kalisz, R. Wejkowski, I. Maj and P. Garbacz, *Energy*, 2023, **279**, 128046.

16 National Energy Technology Laboratory, *Integrated Dry NO$_x$/SO$_2$ Emissions Control System, A DOE Assessment*, 2001.

17 B. Walawska, A. Szymanek and A. Pajdak, *Chemik*, 2013, **67**, 903–912.

18 G. Kresse and J. Furthmüller, *Phys. Rev. B: Condens. Matter Mater. Phys.*, 1996, **54**, 11169–11186.

19 G. Kresse and J. Furthmüller, *Comput. Mater. Sci.*, 1996, **6**, 15–50.

20 J. P. Perdew, K. Burke and M. Ernzerhof, *Phys. Rev. Lett.*, 1996, **77**, 3865–3868.

21 P. E. Blöchl, *Phys. Rev. B: Condens. Matter Mater. Phys.*, 1994, **50**, 17953–17979.

22 Y. Liu, W. Cen, Z. Wu, X. Weng and H. Wang, *J. Phys. Chem. C*, 2012, **116**, 22930–22937.

23 S. Ma, X. Bie, C. Gong, B. Qu and D. Liu, *RSC Adv.*, 2021, **11**, 8846–8856.

24 T. C. Keener and S.-J. Khang, *Chem. Eng. Sci.*, 1993, **48**, 2859–2865.

25 X. Zhang, S. Wang, J. Li, X. Xiao and S. Shu, *Chem. Eng. Sci.*, 2023, **281**, 119157.

26 T. Zhou, Y. Zhao, X. Xiao, Y. Liu, H. Bai, X. Chen, J. Dou and J. Yu, *ACS Omega*, 2022, **7**, 29171–29180.

27 T. Ishizuka, H. Kabashima, T. Yamaguchi, K. Tanabe and H. Hattori, *Environ. Sci. Technol.*, 2000, **34**, 2799–2803.

28 D. Littlejohn and S.-G. Chang, *J. Electron Spectrosc. Relat. Phenom.*, 1995, **71**, 47–50.

29 K. Stejskalová, I. Spirovová, E. Lippert, K. Mocek and Z. Bastl, *Appl. Surf. Sci.*, 1996, **103**, 509–516.

30 B. J. Lindberg, K. Hamrin, G. Johansson, U. Gelius, A. Fahlman, C. Nordling and K. Siegbahn, *Phys. Scr.*, 1970, **1**, 286–298.

31 K. He, S. Su, S. Ding and W. Sun, *React. Kinet., Mech. Catal.*, 2018, **123**, 757–770.

32 H. Peisert, T. Chassé, P. Streubel, A. Meisel and R. Szargan, *J. Electron Spectrosc. Relat. Phenom.*, 1994, **68**, 321–328.

33 S. Enami, C. D. Vecitis, J. Cheng, M. R. Hoffmann and A. J. Colussi, *J. Phys. Chem. A*, 2007, **111**, 13032–13037.

34 K. Burger, F. Tschismarov and H. Ebel, *J. Electron Spectrosc. Relat. Phenom.*, 1977, **10**, 461–465.

35 M. Datta, H. J. Mathieu and D. Landolt, *Appl. Surf. Sci.*, 1984, **18**, 299–314.

36 Á. Vegas, J. F. Liebman and H. D. B. Jenkins, *Acta Crystallogr., Sect. B: Struct. Sci.*, 2012, **68**, 511–527.

37 M. C. Paganini, M. Chiesa, P. Martino, E. Giamello and E. Garrone, *J. Phys. Chem. B*, 2003, **107**, 2575–2580.